Journal of Materials Chemistry C

PAPER

View Article Online
View Journal | View Issue

Cite this: J. Mater. Chem. C, 2018, 6, 2822

Flexible room-temperature volatile organic compound sensors based on reduced graphene oxide–$WO_3 \cdot 0.33H_2O$ nano-needles†

Tarcísio M. Perfecto, [a] Cecilia A. Zito, [a] Talita Mazon [b] and Diogo P. Volanti *[a]

Received 19th January 2018,
Accepted 15th February 2018

DOI: 10.1039/c8tc00324f

rsc.li/materials-c

Flexible sensors have attracted significant attention due to their currently desirable properties and possibility to be applied to any surface and conditions such as wearable electronic devices. Therefore, we prepared volatile organic compound (VOC) sensors based on $WO_3 \cdot 0.33H_2O$ nano-needles and their composites with reduced graphene oxide (RGO) on flexible polyethylene terephthalate (PET) substrates. The materials were synthesized *via* a combination of the ultrasonic spray nozzle (USN) and microwave-assisted hydrothermal (MAH) methods to obtain a single $WO_3 \cdot 0.33H_2O$ orthorhombic crystalline phase. The VOC sensing properties of the materials deposited on PET electrodes were studied at room temperature (22 °C) and 55% relative humidity. The materials were exposed to acetone, ethanol, isopropanol, acetic acid, and methanol to determine their selectivity. The materials exhibited a good selectivity for isopropanol. The 5%RGO–$WO_3 \cdot 0.33H_2O$ composite presented a superior isopropanol-sensing performance, with a response of 4.96 to 100 ppm, which was ~1.6 times higher than that of the pure $WO_3 \cdot 0.33H_2O$ nano-needles. The materials behaved as p-type semiconductors due to an inversion of the sensitive layer promoted by the adsorption of water molecules on the surface of the material.

Introduction

The demand for volatile organic compound (VOC) sensors has increased, and with this increase comes the advancement in wearable electronic technology and applicability of these sensors. These advances include flexible sensors which has promoted simple solutions for the application of sensors in multiple conditions, surfaces and purposes, such as in industrial production, health-care, disease diagnosis, epidermal sensor and environmental monitoring.[1–6] One of the flexible materials used as a sensor substrate is polyethylene terephthalate (PET). PET is of great interest because it has excellent adhesion properties to different materials, is versatile, has good thermal stability (up to approximately 150 °C), is chemically stable, transparent, and recyclable.[2,7,8]

Flexible sensors can be realized by preparing interdigitated electrodes on PET substrates and then adding the sensing material.[9] Among the sensing materials, tungsten trioxide (WO_3) has demonstrated great potential as a gas sensor.[10–13] The advantages of WO_3 include its high sensitivity and selectivity for VOCs.[14,15] However, the sensing properties depend on high operating temperatures.[16,17] In addition, WO_3 has several crystalline phases and forms of hydrates, including $WO_3 \cdot 0.33H_2O$, $WO_3 \cdot H_2O$, and $WO_3 \cdot 2H_2O$.[18–20] The crystalline hydrate $WO_3 \cdot 0.33H_2O$, in particular, has shown great VOC-sensing performance at room temperature.[13,21]

Different strategies have been proposed to improve the gas sensing performance of WO_3, such as selectivity, sensitivity and low operating temperatures. Composites with graphene and WO_3 have demonstrated outstanding sensing performance due to their synergistic effects.[22,23] Besides, the gas-sensing characteristics are strongly dependent on the synthetic method.[12,21] However, few studies have been conducted concerning the effects of the synthesis route and graphene modification on the VOC-sensing performance of $WO_3 \cdot 0.33H_2O$ at room temperature using flexible sensors on PET substrates.

Thereby, in this work, we propose the preparation of flexible sensors on PET substrates with silver interdigitated electrodes based on RGO–$WO_3 \cdot 0.33H_2O$ composites, synthesized using a combination of ultrasonic spray nozzle (USN) and microwave-assisted hydrothermal methods (MAH). The flexible sensors were first prepared by printing silver interdigitated electrodes on PET sheets, and then the sensing materials were deposited.

[a] Laboratory of Materials for Sustainability (LabMatSus), Ibilce, São Paulo State University (Unesp), R. Cristóvão Colombo, 2265, S. J. Rio Preto, SP, 15054-000, Brazil. E-mail: volanti@ibilce.unesp.br
[b] Center for Information Technology Renato Archer (CTI), Rod. D. Pedro I, KM 143,6, Campinas, SP, 13069-901, Brazil

† Electronic supplementary information (ESI) available. See DOI: 10.1039/c8tc00324f

The flexible sensors showed excellent VOC sensing performance under humidity and at room temperature (22 °C). The materials presented a high sensitivity and selectivity for isopropanol, and the addition of 5%RGO in the structures based on $WO_3{\cdot}0.33H_2O$ caused a drastic increase in response.

Experimental section

Synthesis of materials

For the synthesis of the RGO–$WO_3{\cdot}0.33H_2O$ composites, different amounts of graphite oxide were used, corresponding to 1% (3.3 mg), 5% (16.5 mg) and 10% (30 mg) relative to the mass of the salt. The graphite oxide (synthesized by a modified Hummers' method)[13] and 1 mmol $Na_2WO_4{\cdot}2H_2O$ (Sigma-Aldrich, >99%) were added in 20 mL deionized water (Millipore 18.2 MΩ cm) and stirred for 15 min. Afterwards, the mixture was immersed into an ultrasonic bath for 1 h for the exfoliation of graphite oxide, to promote the formation of graphene oxide (GO). Then, the mixture was transferred to the syringe and sprayed into a 0.5 mol L^{-1} HCl solution (Sigma-Aldrich, >37%) and kept under stirring for 15 min, as described in our previous work.[21] The dark and turbid solution was transferred to a polytetrafluoroethylene (PTFE) reactor with a stainless-steel seal and heated in the microwave system at 160 °C for 1 h. After the synthesis was complete, the reactor was cooled at room temperature. The powders were collected and centrifuged at 7000 rpm, washed with deionized water 3 times and once with ethanol. Finally, the samples were dried at 80 °C for 2 h. The synthesized samples were labeled as 1%RGO–$WO_3{\cdot}0.33H_2O$, 5%RGO–$WO_3{\cdot}0.33H_2O$ and 10%RGO–$WO_3{\cdot}0.33H_2O$. For comparison, a pure $WO_3{\cdot}0.33H_2O$ sample was synthesized following the same procedure, except for the addition steps of GO and ultrasonic bath.

Characterization

X-ray diffraction (XRD) was performed to characterize the crystalline and structural properties. A Rigaku X-ray diffractometer, a Mini Flex 300 model, operating with Cu Kα = 1.54184 Å and an incident angle with the surface (2θ) of 10 to 70°, 30 kV and 10 mA was used for this purpose. For the study of the chemical vibrations and composition of the samples, Fourier-transform infrared spectroscopy (FTIR) was performed using an infrared spectrophotometer with attenuated total reflectance, a Perkin Elmer brand was used, operating in the region of 400–4000 cm^{-1}, with a resolution of 2 cm^{-1}.

The thermal stability of the materials was studied by thermogravimetric (TG) analysis using a Perkin-Elmer thermal analyzer, model TGA 4000, a heating rate of 50 °C min^{-1} in the temperature range of 50 °C to 800 °C under a N_2 atmosphere with a flow rate of 20 mL min^{-1}. The bonding vibrations of the crystalline structure of the material and RGO were studied using a Raman HORIBA T64000 triple grid spectrometer with 633 nm laser excitation. X-ray photoelectron spectroscopy (XPS) was performed using a Thermo Scientific K-Alpha X-ray Photoelectron Spectrometer, using Al Kα radiation (1486.6 keV) calibrated with reference to the C 1s peak. The morphology and structural characteristics of the material were studied using a field emission gun scanning electron microscope (FESEM) JEOL, model JSM-7500F operated with an acceleration voltage of 5 kV, and a transmission electronic microscope (TEM) of the brand FEI Tecnai, model G2 F20, operated at an acceleration voltage of 200 kV. Measurement of the specific surface area was performed by the Brunauer–Emmett–Teller (BET) method using a Gemini VII Surface Area and Porosity Analyzer (Micromeritics). X-ray absorption spectroscopy (XAS) data were obtained at the W L_3-edge at the dispersive X-ray beamline D06A-DXAS, LNLS-CNPEM (National Laboratory of Synchrotron Light, Brazil) equipped with a focusing curved Si(111) monochromator operating in Bragg mode for the selection of the desired X-ray wavelength range (10 000–10 500 eV).

Interdigital fabrication and sensor preparation

To print the silver interdigitated electrodes on PET, the Dimatix inkjet printer cartridge was filled with silver ink (Dupont PE410). The cartridge was attached to the printer, and PET sheets were used for printing. After printing, the silver ink was dried and cured in a vacuum oven at 100 °C for 12 h, revealing the interdigital electrodes. The powders of the synthesized materials were dispersed using an ultrasonic bath for 10 min. Then, the dispersion was deposited on the PET substrates with interdigitated electrodes, under heating at 100 °C. The prepared sensor was heated to 150 °C for 15 min for better adhesion and accommodation between tracks and for the removal of any solvent residues and moisture. The images of the printing process and the final printed electrodes are depicted in Fig. S1 (ESI†).

Gas-sensing measurement

An apparatus was set up to carry out the VOC-sensing measurements of the material at room temperature. The system consists of an air flow passing through a recipient containing a saturated solution of NaBr, promoting a controlled relative humidity (RH) of ~55%, and finally, the flow passes through the chamber containing the sensor, thus forming the baseline. For VOC injection, the flow is interrupted, and then with the aid of a syringe, the VOC of known concentration is injected into the chamber. The change in resistance promoted by the sensor reactions with the VOC is measured using a Keithley 2400 instrument, applying a voltage of 2 V, and this signal is converted *via* software into a time-by-resistance graph. The RH of the airflow is measured using a thermohygrometer (HANNA HI 9564). The sensor performance was studied by exposing the materials to different concentrations of VOCs (1–200 ppm). The sensor response for reducing gases is defined as the ratio of gas and air resistance (R_{gas}/R_{air}).

Results and discussion

Fig. 1 depicts the XRD patterns of the pure sample and the RGO composites. The $WO_3{\cdot}0.33H_2O$ orthorhombic single phase was indexed for all materials (JCPDS 72-199). It was not possible to index any diffraction peak corresponding to the RGO due to the

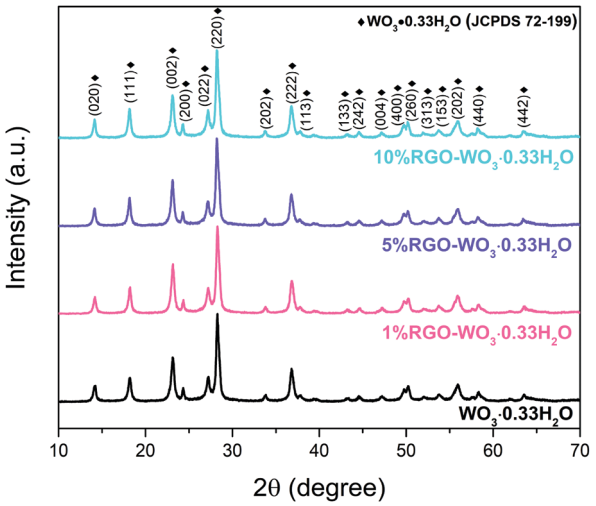

Fig. 1 XRD patterns of the pure sample and RGO–WO_3·0.33H_2O composites.

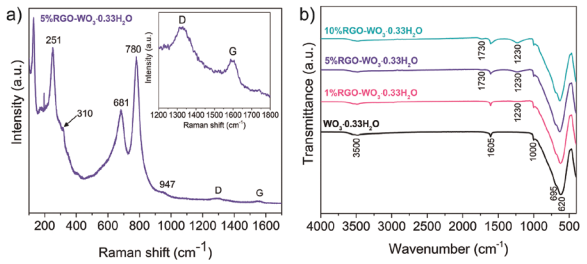

Fig. 2 (a) Raman spectrum of 5%RGO–WO_3·0.33H_2O, and the inset of the region of D and G bands of RGO. (b) FTIR spectra of 1, 5 and 10%RGO–WO_3·0.33H_2O composites in comparison to the pure sample.

small amounts of the material present in the samples. The RGO incorporation does not change the WO_3·0.33H_2O crystalline phase, retaining the orthorhombic phase. In addition, no peaks corresponding to secondary phases or impurities were identified, confirming the purity of the material.

Fig. 2a shows the Raman spectrum of the sample of 5%RGO–WO_3·0.33H_2O. In the broad spectrum of Fig. 2a, it is possible to assign the low-intensity band at ~947 cm^{-1} to the terminal mode stretch of the W=O bond. The bands at 780 and 681 cm^{-1} can be attributed to the vibrational stretching of the oxygen bonds. The peaks at 310 and 251 cm^{-1} are located in the region of the vibrations of ν(W–OH_2), δ(O–W–O) and ν(W–O–W).[24,25] The inset of Fig. 2a shows the region between 1200 and 1800 cm^{-1}, where it is possible to see the characteristic bands of graphene-based materials. The D band (1250 to 1400 cm^{-1}) is due to structural imperfections in the A_{1g} mode, and the G band (1500 to 1650 cm^{-1}) results from the dispersion of the first E_{2g} mode.[26–28] The intensity ratio I_D/I_G was 1.56, which is higher than the value of 1.24 for pure GO, reported in our previous study.[29] The increase in the ratio I_D/I_G indicates that GO was significantly reduced to RGO during the MAH synthesis.[30]

The FTIR spectra for the RGO–WO_3·0.33H_2O composites compared to the pure WO_3·0.33H_2O are shown in Fig. 2b. Comparing the FTIR spectra of RGO–WO_3·0.33H_2O composites with the pure sample, it was possible to verify that there are common absorption bands for all samples. The band at the 3500 cm^{-1} region is attributed to the symmetrical vibrational stretching of the O–H intermolecular bond of water.[31] This band comes from the crystallization waters of the material and can also be attributed to adsorbed water. The peak observed for all samples at 1605 cm^{-1} can be attributed to H_2O due to the vibration of the O–H bonds of water. The peak observed at 1000 cm^{-1} corresponds to the short terminal W–O bond of the terminal oxygen and the bands at 695 and 620 cm^{-1} correspond to the vibration of the W–O–W bond.[32] The low-intensity band observed for the 5% and 10%RGO–WO_3·0.33H_2O composites in the 1730 cm^{-1} region is attributed to the vibrational stretch of the C=O bond of the remaining GO functional groups. The band observed in the 1230 cm^{-1} region is attributed to the vibrational stretch of the C–O bond of functional groups.[31]

It is noted that microwave radiation is not sufficient to completely remove the functional groups inserted during graphite oxide synthesis. It is also noted that the higher the concentration of RGO, the higher the intensity of 1230 cm^{-1} bands.

The RGO–WO_3·0.33H_2O composites and the pure samples were analyzed by TG analysis according to Fig. S2 (ESI†). It was possible to evaluate the thermal stability of the samples as well as the presence of crystalline hydrates and RGO in the composites.

With the TG curve, it is possible to observe two mass loss events for the pure sample and three events for the composites. The first mass loss event occurs up to 210 °C. This event is associated with the removal of molecules of water physically adsorbed in the material from the humidity of the air. This mass loss corresponds to 2.3% for the pure sample and ~1.3% for the composites. This difference in mass suggests that the composites have less adsorbed water on their surface which can be linked to an increase in the hydrophobicity of the material. The second mass loss event occurs between 210 and 440 °C. This event is associated with the elimination of water of constitution, which are chemically bound. The water of constitution refers to the crystalline hydrate of the WO_3·0.33H_2O phase and also to the oxygenated functional groups remaining in the RGO, which are eliminated as CO_2 and water. Note that the higher the concentration of RGO, the higher the mass loss in this step, due to the higher number of functional groups, however, it is not higher than the mass loss in the pure sample. The loss of the pure sample was 3.4% at this stage and 1.8, 2.2 and 2.6% for the composites of 1, 5 and 10%RGO–WO_3·0.33H_2O, respectively. The third event of mass loss occurs between 440 and 650 °C, which is evidenced only for the composites, and is associated with the elimination of the carbon skeleton of the RGO, in the form of CO_2. The mass loss for this event for the composites with 1, 5 and 10% of RGO were respectively 0.9, 2.8 and 4.9%.

The elemental composition and chemical states of the elements in the 5%RGO–WO_3·0.33H_2O composite were studied by XPS. The survey spectrum in Fig. 3a shows that the surface composition of the sample consists of W, O, and C. The elements W and O are from the WO_3·0.33H_2O, whereas the element C is

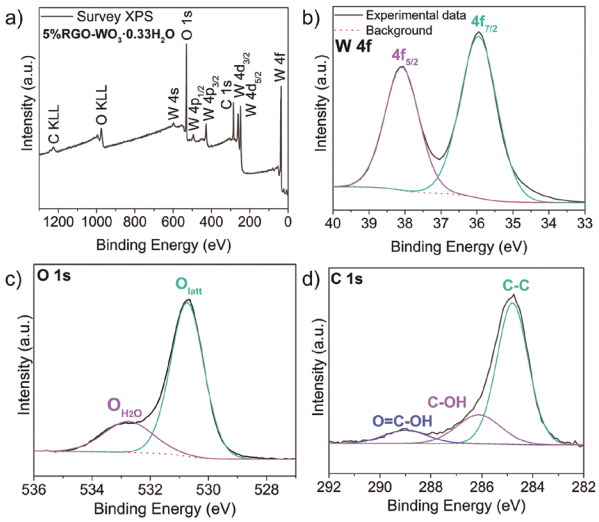

Fig. 3 XPS spectra of 5%RGO–WO_3·0.33H_2O. (a) Survey scan, high-resolution of (b) W 4f, (c) O 1s, and (d) C 1s.

related to the RGO in the composite, corroborating with the results of FTIR and Raman spectroscopy.

Fig. 3b shows the high-resolution spectrum of W 4f. The symmetric peaks at 38.1 and 35.9 eV can be assigned to W $4f_{5/2}$ and W $4f_{7/2}$, respectively.

The high-resolution spectrum of O 1s depicted in Fig. 3c can be fitted in two contributions. The peak at 532.8 eV can be related to the crystal oxygen lattice (Olatt) in WO_3·0.33H_2O (W═O and W–O–W bonds), and the peak at 530.7 eV can be related to the oxygen bonds of water (O_{H_2O}) adsorbed on the surface and crystalline hydrates.

Fig. 3d shows the C 1s XPS spectrum of 5%RGO–WO_3·0.33H_2O. It is possible to note three components in the spectrum at 289.0, 286.2, and 284.8 eV, related to C–C, C–OH, and O–C═O, respectively. Such contributions may be associated with the presence of RGO in the composites. The intensity of the C 1s components associated with carbon–oxygen groups are much lower than those of GO, shown in Fig. S3 (ESI†). The dramatic decrease in the intensities of these components indicates that a great portion of the functional groups of GO were removed during the MAH process.

Fig. 4a shows a photograph of the PET with printed interdigital arrays, elucidating its flexibility. Fig. 4b–d shows the FESEM images of the PET electrode surface after the deposition with the 5%RGO–WO_3·0.33H_2O sample. It is possible to verify that the combination of the methods generates aggregate structures with varied sizes (~280 nm length and ~50 width). The morphology of the material is similar to nano-needles, which agglomerate and form a structure with large areas and cavities. In Fig. 4d, it is possible to see that the RGO sheet acts as a support for the nano-needles and confers interconnectivity of the particles and also as a nucleation site of smaller particles of WO_3·0.33H_2O. The FESEM images of the pure sample and the other composites are displayed in Fig. S4 (ESI†).

TEM analysis of the powders of the 5%RGO–WO_3·0.33H_2O composite was used to further determine the morphology of

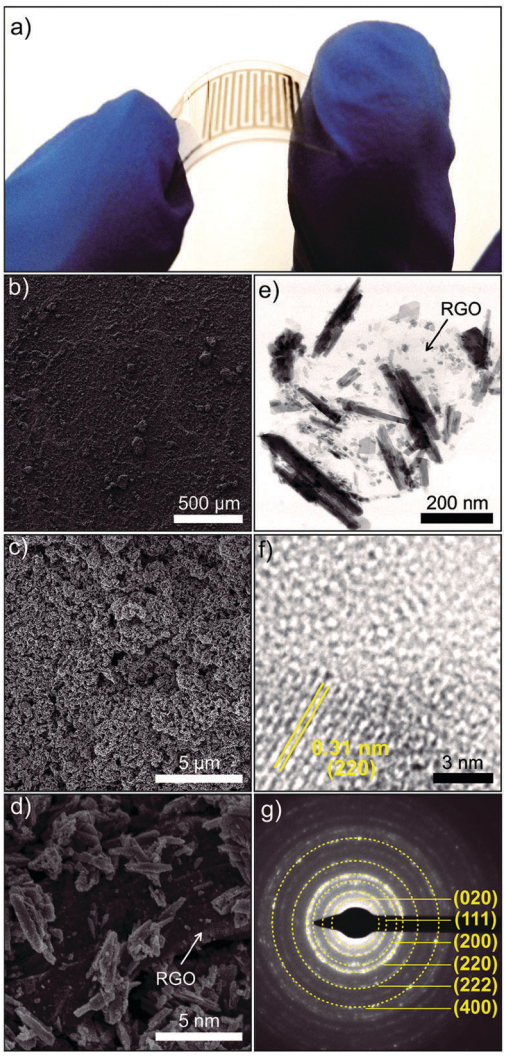

Fig. 4 (a) Photograph of the PET substrate with an interdigital electrode, (b–d) FESEM images of the 5%RGO–WO_3·0.33H_2O sample deposited on the PET interdigitated electrode, (e) the TEM image of the 5%RGO–WO_3·0.33H_2O sample, (f) the HRTEM image of the 5%RGO–WO_3·0.33H_2O sample, and (g) SAED pattern of the 5%RGO–WO_3·0.33H_2O sample.

the material. With the TEM image (Fig. 4e), it was possible to verify that the material is made up of well-defined faceted nano-needles. It is possible to see the RGO as a support for the growth of nano-needles and nucleation sites, evidenced by other smaller structures (Fig. 4e). Dark-field TEM images allow a better visualization of RGO sheets (Fig. S5, ESI†). Fig. 4f shows high-resolution (HR) TEM image of the 5%RGO–WO_3·0.33H_2O sample, being possible to visualize the atomic stacking of the material. The interplanar distance of the atomic plane of 0.31 nm was determined, corresponding to the plane (220) of the orthorhombic phase of WO_3·0.33H_2O. Fig. 4g shows the selected area electron diffraction (SAED) of the 5%RGO–WO_3·0.33H_2O composite. The SAED profile obtained in the form of rings indicates the polycrystalline nature of the sample. It was possible to index the (020), (111), (200), (220), (222) and (400) planes of the orthorhombic phase of WO_3·0.33H_2O, which are in agreement with the XRD results. In addition, no impurities or secondary phases were observed in the analysis.

Specific surface area analysis of the samples was performed by the BET method. The BET surface areas of the materials were 68, 49, 54, and 64 $m^2 g^{-1}$ for pure $WO_3{\cdot}0.33H_2O$, 1% RGO–$WO_3{\cdot}0.33H_2O$, 5% RGO–$WO_3{\cdot}0.33H_2O$ and 10% RGO–$WO_3{\cdot}0.33H_2O$, respectively. The results showed a high surface area in relation to previous work on similar materials.[13] A decrease in the surface area in the composites is evident compared to the pure sample. This is due to the agglomeration of the material on the RGO surface. However, the higher the RGO concentration, the higher the surface area in the composites. This is due to the high surface area characteristic of RGO.[33]

The possible growth mechanism of RGO–$WO_3{\cdot}0.33H_2O$ can be explained in two fundamental steps. The initial nucleation of an agglomerate of H_2WO_4 (tungstic acid) with the GO sheet dispersion promoted by the USN method (Fig. 5a), and then the crystallization of the single orthorhombic crystal phase of $WO_3{\cdot}0.33H_2O$ and reduction of the GO to RGO promoted by the MAH method (Fig. 5b). First, when the solution containing Na_2WO_4 and GO is sprayed, ~35 μm droplets are generated (Fig. 5a-I).[34] The interaction between the droplets and the HCl solution causes the micro-drop break, generating an acid supersaturation around the breaking (Fig. 5a-II). At this time, the droplet acts as a micro-reactor, rapidly nucleating amorphous aggregates of H_2WO_4 in the solution and nanoparticles of H_2WO_4 on the GO surface, due to the adsorption of Na_2WO_4 on its surface. At the end, a GO–H_2WO_4 dispersion (Fig. 5a-III) is formed.

The second step occurs *via* the MAH method (Fig. 5b-I). This stage is critical for the crystallization and formation of the orthorhombic phase of $WO_3{\cdot}0.33H_2O$ at the same time as the reduction of GO to RGO occurs. On MAH conditions, the formation of nano-needles occurs on the surface of RGO. Then, the nano-needles are self-assembled, forming a nano-needle aggregate, covering the RGO sheet, resulting in the composite (Fig. 5b-II).

The first step to verify the sensing performance of the materials was to verify their sensitivity to different VOCs at room temperature (20 °C) and in the presence of humidity (55% RH). Fig. 6 shows the sensing response of the samples to 100 ppm of acetone, ethanol, isopropanol, acetic acid, and methanol. It can be seen that the samples, except for 10%RGO–$WO_3{\cdot}0.33H_2O$, have a good selectivity and excellent sensitivity to isopropanol. The 10%RGO–$WO_3{\cdot}0.33H_2O$ showed a worse sensing performance than the pure sample. Therefore, the excess of RGO concentration in the composites is detrimental to the VOC sensing performance. Moreover, the best RGO concentration in the composites was 5%, showing a response to isopropanol of about 1.85 times higher than the response to acetic acid (the second largest one), while the pure sample exhibited a response of only 1.39 times higher. Thus, the presence of RGO improved the selectivity and sensitivity of the material.

Since pure $WO_3{\cdot}0.33H_2O$ and RGO–$WO_3{\cdot}0.33H_2O$ composites presented better sensitivity and selectivity for isopropanol vapor, the isopropanol response was evaluated at the concentrations of 1, 10, 50, 100 and 200 ppm (Fig. 7).

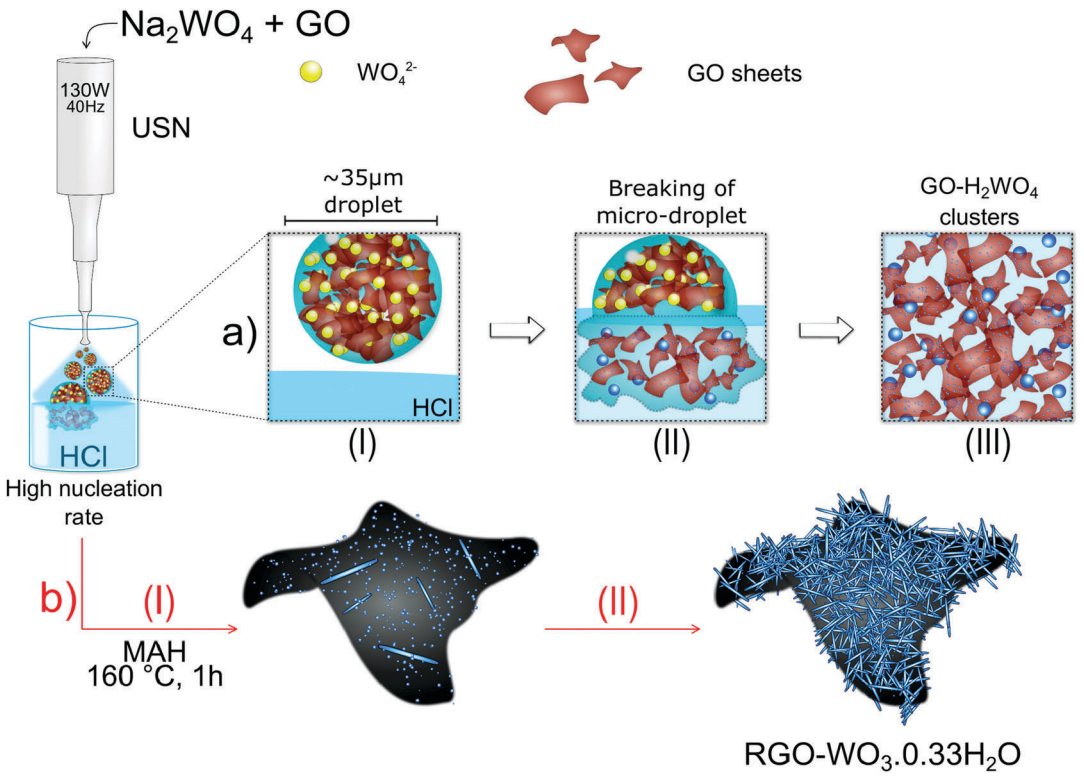

Fig. 5 Scheme of growth and formation of RGO–$WO_3{\cdot}0.33H_2O$ by the combination of USN and MAH methods. (a) Formation of GO-H_2WO_4 aggregates promoted by the USN method, (b) crystallization of the orthorhombic phase of $WO_3{\cdot}0.33H_2O$ and reduction of GO to RGO and the formation of the RGO–$WO_3{\cdot}0.33H_2O$ composite by the MAH method.

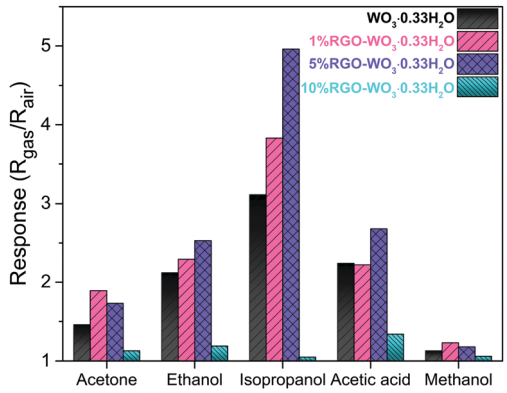

Fig. 6 Sensing response to 100 ppm of different VOCs of the pure sample and the RGO–WO_3·0.33H_2O composites.

The graph shown in Fig. 7a indicates that the 5%RGO–WO_3·0.33H_2O sample has the best sensitivity, presenting a higher response than the pure sample for all isopropanol concentrations. The response of 5% RGO–WO_3·0.33H_2O to 100 ppm of isopropanol was 4.96, which was ~1.6 times higher than that of the pure WO_3·0.33H_2O. Interestingly, the 10%RGO–WO_3·0.33H_2O sample presents low response to isopropanol. Therefore, the high concentration of RGO drastically affected the response of the material, which had a much lower response than the other samples. This can be explained by the RGO wrapping the WO_3·0.33H_2O active sites, which are responsible for the sensing response of the material.[35] Therefore, there is a significant decrease in the electrical resistance, reducing its response drastically (Fig. S6, ESI†). In Fig. 7b, the graphs of time in function of the resistance collected during the exposure of the 5%RGO–WO_3·0.33H_2O sample to isopropanol are presented. We can see an increase in the signal with increasing concentration of isopropanol. The moment of injection of the VOC and the moment the air flow is on for cleaning are shown in Fig. 7c. We can conclude that the superior response of the 5%RGO–WO_3·0.33H_2O composite is not because of an increase in the surface area, but due to the p–n type junction between the two materials, RGO and WO_3, resulting in a synergistic effect, and, thus improving the VOC sensing performance of the material. In addition, the sensor also showed a distinct response to isopropanol concentrations as low as 1 ppm, indicating that it has a low limit of detection (LOD) in the ppm range for detecting isopropanol. The LOD was determined to be approximately 1 ppm.

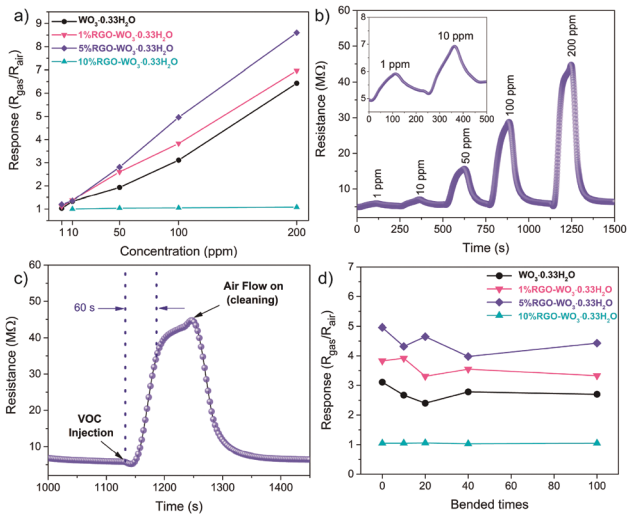

Fig. 7 (a) Comparison of the responses to isopropanol for all synthesized samples, (b) resistance *versus* time plot of the 5%RGO–WO_3·0.33H_2O sample, (c) moments of VOC injection and air flow on, and (d) performance of the sensor under bending tests.

The flexible sensors were subjected to bending tests to study the mechanical stability. The response to 100 ppm of isopropanol was measured after the sensor was bent 10, 20, 40 and 100 times under a bending angle of 90°, as shown in Fig. 7d. The results show that the sensors did not have their performance affected by the bending.

The response values remained almost constant, indicating the reliable flexibility of the prepared sensors.

The response time (the time required to reach 90% maximum response) was calculated for all samples and is shown in Fig. S7 (ESI†). For the best sensor composition (5%RGO–WO_3·0.33H_2O), the response time ranged from 90 to 60 s to the isopropanol concentration range of 1–200 ppm. Such response times are relatively short, considering the operation at room temperature and in the presence of humidity.

Table 1 lists the properties of various materials as isopropanol sensors reported in the literature. The isopropanol sensor based on 5%RGO–WO_3·0.33H_2O showed excellent sensitivity, taking into consideration the working temperature and the operation in the presence of 55% RH. The highlight of our sensor is the flexible PET substrates. None of the reported isopropanol sensors use this kind of substrate.

In addition, while the reported sensors require temperatures higher than 230 °C, the material in this work has its operation at room temperature, with an enhanced sensitivity. The improved sensing properties are due to the synthesis method to produce the composite, promoting an excellent interconnectivity between RGO and WO_3·0.33H_2O nanoneedles, and the ideal RGO concentration.

Fig. 7b shows that the electrical resistance of the material increases when exposed to the reducing VOC, characteristic of p-type semiconductors, however, WO_3 is an n-type semiconductor.

Table 1 Comparison of the isopropanol sensing properties of different materials

Materials	Conc. (ppm)	Temp. (°C)	RH (%)	Sensor response[a]	Ref.
WO_3·0.33H_2O nanocolumns	100	Room temp.	55	3.4	21
SnO_2 nanorods	100	255	50	4.7	39
SnO_2 nanorings	100	250	Dry	7.27	40
ZnO nanoparticles	150	250	Dry	1.85	41
TiO_2 nanoparticles	200	300	Dry	1.68	42
CuO particles	190	230	Dry	2.6	43
5%RGO–WO_3·0.33H_2O	100	Room temp.	55	4.96	This work

[a] Sensor response defined as R_{gas}/R_{air} or R_{air}/R_{gas}.

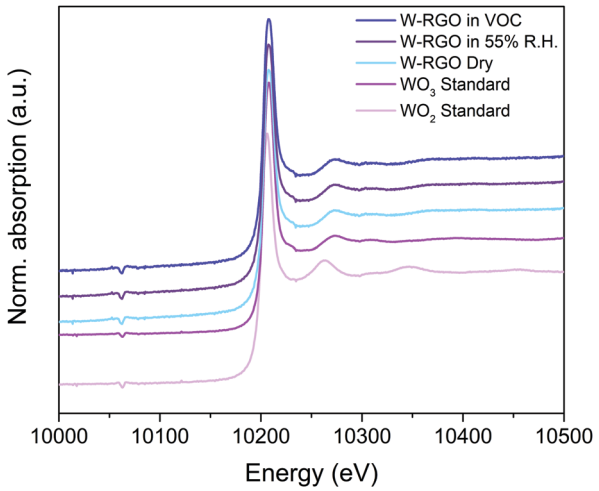

Fig. 8 XAS spectra at the W-L_3 edge of WO_2 and WO_3 as references compared to the 5%RGO–WO_3·0.33H_2O sample under dry and wet air conditions, and in the presence of isopropanol.

To understand the observed effect, the 5%RGO–WO_3·0.33H_2O sample was subjected to measurements with XAS. This study allows inferring if the interactions of the VOC and humidity with the surface of the sensor material promote alterations in the oxidation states or electronic modifications. Fig. 8 shows the XAS spectra at the W-L_3 edge of WO_2 (+4) and WO_3 (+6) standards compared to the sample of 5%RGO–WO_3·0.33H_2O (referred to as W-RGO in the figure) under dry and wet air flow conditions and after isopropanol exposure (200 ppm). The XAS spectrum for the W-L_3 edge shows a peak, called the white line (WL), at 10 206 eV, just above the absorption edge, a result that is consistent with that presented in the literature.[36]

This peak is attributed to the transition of the photoelectron between the $2p_{3/2}$ state and the final 5d state.[37] The lower the oxidation state, the lower the energy required to excite the electron, so the edge position is extremely related to the oxidation state.[38] No significant changes were observed in XANES (X-ray absorption near edge structure) regions of the XAS spectra, all the spectra of the studied sample under conditions of humidity and VOC presented the same intensity and position. We conclude that the propensity of the material to work as a useful sensor for isopropanol does not depend on modifications of its electronic structure or changes in the oxidation state, and is also not responsible for the inversion of p–n type of the response.

Thus, we propose an explanation for this inversion based on the literature where this inversion effect has already been observed and explained by the adsorption of water species and oxygen species at room temperature, forming an inverse sensitive layer, which respond to VOCs as a p-type semiconductor.[13,44] The possible sensor mechanism is exemplified in Fig. 9.

The semiconductor material in its initial state is exposed to an air flow with humidity, resulting in the sorption of oxygen (O_2, O_2^-, O^-, O^{2-} e/ou O_2^{2-})[45] and water as OH. The oxygen species act as electron acceptors forming a depletion layer on the surface of the material (insulating layer) and water acts as an electron donor, forming a conductive inversion layer, as

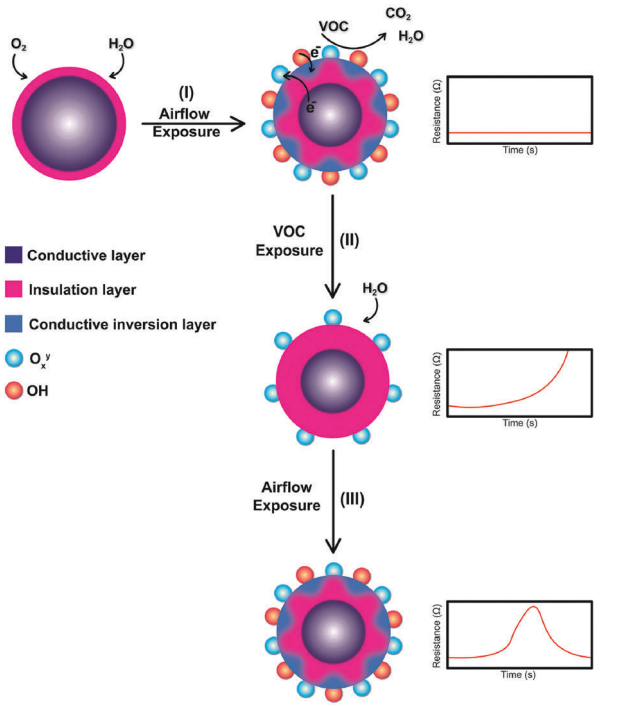

Fig. 9 Proposed sensor mechanism for the inversion of n-type response to p-type of the WO_3·0.33H_2O semiconductor.

proposed in the literature (Fig. 9-I). Thus, when the material is exposed to a VOC (Fig. 9-II), it reacts with the material consuming oxygen species (oxidizing the volatile organic compounds producing CO_2 and water) and removing the adsorbed water, decreasing the conductive inversion layer, the resistance increases and the material present p-type semiconductor behavior. Finally, when exposing the material to the air flow with humidity, the material returns to its initial state (Fig. 9-III).

Conclusions

Combining the USN and MAH methods, we synthesized WO_3·0.33H_2O nano-needles and their RGO–WO_3·0.33H_2O composites with different RGO amounts. The growth of WO_3·0.33H_2O nano-needles occurred on the RGO surface, conferring a great interconnectivity between them. The materials were deposited on the PET substrates with interdigitated electrodes and their VOC-sensing properties were investigated at room temperature and 55%RH. The VOC-sensing studies revealed that the 5%RGO–WO_3·0.33H_2O composite was the most sensitive and selective composition, whereas the high RGO concentration in the composites (10%RGO–WO_3·0.33H_2O) had a detrimental effect on the sensing performance. The 5%RGO–WO_3·0.33H_2O composite exhibited an enhanced isopropanol-sensing performance, including sensitivity and selectivity, compared to pure WO_3·0.33H_2O. This can be attributed to the p–n type heterojunction between RGO and WO_3·0.33H_2O nano-needles, resulting in a synergistic effect. Therefore, the ideal concentrations of RGO along WO_3·0.33H_2O nano-needles have great potential for the application as flexible VOC sensors under real operating conditions.

Conflicts of interest

There are no conflicts to declare.

Acknowledgements

The authors acknowledge financial support from the São Paulo Research Foundation – FAPESP (grant 2016/04371-1, 2017/01267-1, 2016/25267-8 and 2013/23886-4), and the National Council for Scientific and Technological Development – CNPq (grant 444926/2014-3). The XPS facilities were provided by the Brazilian Nanotechnology National Laboratory – LNNano/CNPEM (proposal 21594). FESEM and TEM facilities were provided by LME/IQ/Unesp and LCE/Dema/UFSCar, respectively. The XAS facilities were provided by the National Laboratory of Synchrotron Light – LNLS/CNPEM at the beamline D06A-XAS (proposal 20170049).

References

1 E. Singh, M. Meyyappan and H. S. Nalwa, *ACS Appl. Mater. Interfaces*, 2017, **9**, 34544–34586.
2 U. Yaqoob, D.-T. Phan, A. S. M. I. Uddin and G.-S. Chung, *Sens. Actuators, B*, 2015, **221**, 760–768.
3 N. Kahn, O. Lavie, M. Paz, Y. Segev and H. Haick, *Nano Lett.*, 2015, **15**, 7023–7028.
4 P. Kuberský, T. Syrový, A. Hamáček, S. Nešpůrek and J. Stejskal, *Procedia Eng.*, 2015, **120**, 614–617.
5 S. Ammu, V. Dua, S. R. Agnihotra, S. P. Surwade, A. Phulgirkar, S. Patel and S. K. Manohar, *J. Am. Chem. Soc.*, 2012, **134**, 4553–4556.
6 S. Yang, Y.-C. Chen, L. Nicolini, P. Pasupathy, J. Sacks, B. Su, R. Yang, D. Sanchez, Y.-F. Chang, P. Wang, D. Schnyer, D. Neikirk and N. Lu, *Adv. Mater.*, 2015, **27**, 6423–6430.
7 Z. Q. Zheng, J. D. Yao, B. Wang and G. W. Yang, *Sci. Rep.*, 2015, **5**, 11070.
8 K. Na, H. Ma, J. Park, J. Yeo, J. U. Park and F. Bien, *IEEE Sens. J.*, 2016, **16**, 5003–5009.
9 R. Li, K. Jiang, S. Chen, Z. Lou, T. Huang, D. Chen and G. Shen, *RSC Adv.*, 2017, **7**, 52503–52509.
10 J. Shin, S. J. Choi, D. Y. Youn and I. D. Kim, *J. Electroceram.*, 2012, **29**, 106–116.
11 Z. Hua, PhD thesis, Kyushu University, 2014.
12 H. Zhang, Z. Liu, J. Yang, W. Guo, L. Zhu and E. W. Zheng, *Mater. Res. Bull.*, 2014, **57**, 260–267.
13 T. M. Perfecto, C. A. de Zito and D. P. Volanti, *RSC Adv.*, 2016, **6**, 105171–105179.
14 N.-H. Kim, S.-J. Choi, S.-J. Kim, H.-J. Cho, J.-S. Jang, W.-T. Koo, M. Kim and I.-D. Kim, *Sens. Actuators, B*, 2016, **224**, 185–192.
15 S.-J. Choi, C. Choi, S.-J. Kim, H.-J. Cho, S. Jeon and I.-D. Kim, *RSC Adv.*, 2014, **5**, 7584–7588.
16 M. Yin, L. Yu and S. Liu, *J. Alloys Compd.*, 2017, **696**, 490–497.
17 S.-J. Choi, S. Chattopadhyay, J. J. Kim, S.-J. Kim, H. L. Tuller, G. C. Rutledge and I.-D. Kim, *Nanoscale*, 2016, **8**, 9159–9166.
18 B. Gerand, G. Nowogrocki and M. Figlarz, *J. Solid State Chem.*, 1981, **38**, 312–320.
19 B. Miao, W. Zeng, Y. Mu, W. Yu, S. Hussain, S. Xu, H. Zhang and T. Li, *Appl. Surf. Sci.*, 2015, **349**, 380–386.
20 S. Ayyappan and N. Rangavittal, *Bull. Mater. Sci.*, 1997, **20**, 103–109.
21 T. M. Perfecto, C. A. Zito and D. P. Volanti, *CrystEngComm*, 2017, **19**, 2733–2738.
22 X. Jie, D. Zeng, J. Zhang, K. Xu, J. Wu, B. Zhu and C. Xie, *Sens. Actuators, B*, 2015, **220**, 201–209.
23 Y. Gui, Z. Liu, S. Fang, J. Tian and F. Gong, *J. Mater. Sci.: Mater. Electron.*, 2016, **27**, 2890–2895.
24 M. F. Daniel, B. Desbat, J. C. Lassegues, B. Gerand and M. Figlarz, *J. Solid State Chem.*, 1987, **67**, 235–247.
25 M. Gotić, M. Ivanda, S. Popović and S. Musić, *Mater. Sci. Eng., B*, 2000, **77**, 193–201.
26 M.-S. Kim, H.-K. Kim, S.-W. Lee, D.-H. Kim, D. Ruan, K. Y. Chung, S. H. Lee, K. C. Roh and K.-B. Kim, *Sci. Rep.*, 2016, **6**, 26686.
27 C. A. Zito, T. M. Perfecto and D. P. Volanti, *Sens. Actuators, B*, 2017, **244**, 466–474.
28 B. A. Vessalli, C. A. Zito, T. M. Perfecto, D. P. Volanti and T. Mazon, *J. Alloys Compd.*, 2017, **696**, 996–1003.
29 C. A. C. A. Zito, T. M. T. M. Perfecto and D. P. D. P. Volanti, *Sens. Actuators, B*, 2017, **244**, 466–474.
30 H. Meng, W. Yang, K. Ding, L. Feng and Y. Guan, *J. Mater. Chem. A*, 2015, **3**, 1174–1181.
31 R. M. Silverstein, F. X. Webster, D. J. Kiemle and D. L. Bryce, *Spectrometric Identification of Organic Compounds*, 2014.
32 A. Chemseddine, F. Babonneau and J. Livage, *J. Non-Cryst. Solids*, 1987, **91**, 271–278.
33 S. Basu and P. Bhattacharyya, *Sens. Actuators, B*, 2012, **173**, 1–21.
34 R. J. Lang, *J. Acoust. Soc. Am.*, 1962, **34**, 6–8.
35 L. Chen, L. Huang, Y. Lin, L. Sai, Q. Chang, W. Shi and Q. Chen, *Sens. Actuators, B*, 2018, **255**, 1482–1490.
36 Y. Zhou, K. Zheng, J. Grunwaldt, T. Fox, L. Gu, X. Mo, G. Chen and G. R. Patzke, *J. Phys. Chem. C*, 2011, **115**, 1134–1142.
37 S. Yamazoe, Y. Hitomi, T. Shishido and T. Tanaka, *J. Phys. Chem. C*, 2008, **112**, 6869–6879.
38 G. Poirier, M. Nalin, Y. Messaddeq and S. J. L. Ribeiro, *Solid State Ionics*, 2007, **178**, 871–875.
39 D. Hu, B. Han, S. Deng, Z. Feng, Y. Wang, J. Popovic, M. Nuskol, Y. Wang and I. Djerdj, *J. Phys. Chem. C*, 2014, **118**, 9832–9840.
40 S. H. Li, Z. Chu, F. F. Meng, T. Luo, X. Y. Hu, S. Z. Huang and Z. Jin, *J. Alloys Compd.*, 2016, **688**, 712–717.
41 C. S. Prajapati and P. P. Sahay, *Sens. Actuators, B*, 2011, **160**, 1043–1049.
42 P. Das, B. Mondal and K. Mukherjee, *Mater. Res. Express*, 2017, **4**, 15503.
43 S. Xia, H. Zhu, H. Cai, J. Zhang, J. Yu and Z. Tang, *RSC Adv.*, 2014, **4**, 57975–57982.
44 Y.-Q. Wu, M. Hu and X.-Y. Wei, *Chin. Phys. B*, 2014, **23**, 40704.
45 A. Martin, *Angew. Chem., Int. Ed.*, 2012, **51**, 2810.